FREQUENCY DOMAIN ELASTIC WAVEFORM INVERSION USING THE GAUSS-NEWTON METHOD

WOOKEEN CHUNG[1], JUNGKYUN SHIN[2], HO SEUK BAE[2*], DONGWOO YANG[3] and CHANGSOO SHIN[2]

[1] *Department of Energy and Resources Engineering, Korea Maritime University, Busan 606-791, South Korea.*
[2] *Department of Energy Systems Engineering, Seoul National University, Seoul 151-742, South Korea. css@model.snu.ac.kr*
[3] *Western Australian Energy Research Alliance, Kensington WA 6151, Australia.*
[*] *Present address: Agency for Defense Development, P.O. Box 18, Jinhae, Changwon 645-600, South Korea.*

(Received August 3, 2011; revised version accepted November 12, 2011)

ABSTRACT

Chung, W., Shin, J., Bae, H.S., Yang, D. and Shin, C.S., 2012. Frequency domain elastic waveform inversion using the Gauss-Newton method. *Journal of Seismic Exploration*, 21: 29-48.

In spite of several advantages of using the Gauss-Newton method for waveform inversion, calculating a Hessian-matrix is problematic in the current computing environment. Consequently, many researchers have suggested a Conjugate Gradient Least Square (CGLS) algorithm to circumvent the Hessian matrix problem in the Gauss-Newton method. There has been no attempt, however, at using the CGLS method to perform elastic media waveform inversion. It is necessary to consider the characteristics of elastic media because the acoustic wave equation does not accurately simulate waveforms propagated through elastic media. Our objective is to develop a frequency domain waveform inversion algorithm using the CGLS method for elastic media. Numerical experiments with the Marmousi-2 model and the SEG/EAGE salt model verify enhancement of the inversion results. We confirm that a greatly improved waveform inversion can be carried out over a complicated layer structure with the Marmousi-2 model. We also verify that structures containing a high velocity salt can be reproduced correctly through an inversion experiment using the SEG/EAGE salt model. However, the improved inversion result of the SEG/EAGE salt model is limited to use with the long wavelength initial velocity, necessitating a method for obtaining the long wavelength velocity model.

KEYWORDS: Gauss-Newton method, conjugate gradient, CGLS, elastic, frequency domain, waveform inversion.

0963-0651/12/$5.00

INTRODUCTION

Waveform inversion is generally derived from the least squares method by iteratively calculating a velocity model to minimize the difference between the observed and the modeled wavefield vector. Since Lailly (1983) and Tarantola (1984) pioneered this field, many researchers have studied waveform inversions with the Gradient method. In the Gradient method, the convergence direction is defined without explicitly calculating a partial differential term that is needed for the waveform inversion. Tarantola (1984) suggested applying the Gauss-Newton method for acoustic waveform inversion. Pratt et al. (1998)

THEORY

Gauss-Newton method

In the frequency domain waveform inversion, the objective function can be defined as

$$E = \tfrac{1}{2}[(\mathbf{u} - \mathbf{d})^T(\mathbf{u} - \mathbf{d})^*] \quad , \tag{1}$$

where the superscript T denotes the transpose of a matrix, the superscript * denotes the complex conjugate operator, and **u** and **d** represent the modeled and observed wavefield vectors, respectively. The aim of the waveform inversion is to obtain the model parameter vector **p** that minimizes the objective function. In this research, we develop a waveform inversion algorithm based on the Gauss-Newton method and present more accurate solutions than those achieved with the Gradient method.

To use the Gauss-Newton method, the modeled wavefield vector **u** can be expanded to its first order Taylor series term:

$$E = \tfrac{1}{2}[(\mathbf{u}_0 + \mathbf{J}\Delta\mathbf{p} - \mathbf{d})^T(\mathbf{u}_0 + \mathbf{J}\Delta\mathbf{p} - \mathbf{d})^* \quad , \tag{2}$$

In eq. (2), $\mathbf{u}_0$ is the modeled wavefield vector using an initial velocity model, **J** is the Jacobian matrix representing the sensitivity of modeled wavefield vector matrix with respect to the modeled parameters, and $\Delta\mathbf{p}$ is a perturbation vector of the modeled parameters such as P-wave velocity, S-wave velocity, and density.

We differentiate eq. (2) with respect to and set it equal to zero to solve the value of that minimizes the objective function. This can be written as

$$\mathbf{J}^T\mathbf{J}^*\Delta\mathbf{p} = -\mathbf{J}^T\mathbf{e}_0 \quad , \tag{3}$$

where $\mathbf{J}^T\mathbf{J}^*$ is the Hessian matrix and $\mathbf{e}_0 = \mathbf{d} - \mathbf{u}_0$. We can obtain $\Delta\mathbf{p}$ by solving the least squares problem in eq. (3) and update each model parameter iteratively. This is the Gauss-Newton method.

The waveform inversion using the Gauss-Newton method suggests a more accurate solution than the Gradient method because it uses a more precise Hessian matrix and less iteration. However, to use the Gauss-Newton method, the approximate-Hessian should be calculated, which is computationally prohibitive in the current computing environment. Even in an improved computing environment, it would take an impractically long time to calculate the approximate-Hessian.

Implementation of the CGLS method

To use the CGLS method, eq. (3) can be rewritten as

$$\begin{bmatrix} \frac{\partial u_1}{\partial v_{p_1}} & \cdots & \frac{\partial u_1}{\partial v_{p_m}} & \frac{\partial u_1}{\partial v_{s_1}} & \cdots & \frac{\partial u_1}{\partial v_{s_m}} & \frac{\partial u_1}{\partial \rho_1} & \cdots & \frac{\partial u_1}{\partial \rho_m} \\ \frac{\partial u_2}{\partial v_{p_1}} & \cdots & \frac{\partial u_2}{\partial v_{p_m}} & \frac{\partial u_2}{\partial v_{s_1}} & \cdots & \frac{\partial u_2}{\partial v_{s_m}} & \frac{\partial u_2}{\partial \rho_1} & \cdots & \frac{\partial u_2}{\partial \rho_m} \\ \vdots & \ddots & \vdots & \vdots & \ddots & \vdots & \vdots & \ddots & \vdots \\ \frac{\partial u_r}{\partial v_{p_1}} & \cdots & \frac{\partial u_r}{\partial v_{p_m}} & \frac{\partial u_r}{\partial v_{s_1}} & \cdots & \frac{\partial u_r}{\partial v_{s_m}} & \frac{\partial u_r}{\partial \rho_1} & \cdots & \frac{\partial u_r}{\partial \rho_m} \end{bmatrix}^T \begin{bmatrix} \frac{\partial u_1}{\partial v_{p_1}} & \cdots & \frac{\partial u_1}{\partial v_{p_m}} & \frac{\partial u_1}{\partial v_{s_1}} & \cdots & \frac{\partial u_1}{\partial v_{s_m}} & \frac{\partial u_1}{\partial \rho_1} & \cdots & \frac{\partial u_1}{\partial \rho_m} \\ \frac{\partial u_2}{\partial v_{p_1}} & \cdots & \frac{\partial u_2}{\partial v_{p_m}} & \frac{\partial u_2}{\partial v_{s_1}} & \cdots & \frac{\partial u_2}{\partial v_{s_m}} & \frac{\partial u_2}{\partial \rho_1} & \cdots & \frac{\partial u_2}{\partial \rho_m} \\ \vdots & \ddots & \vdots & \vdots & \ddots & \vdots & \vdots & \ddots & \vdots \\ \frac{\partial u_r}{\partial v_{p_1}} & \cdots & \frac{\partial u_r}{\partial v_{p_m}} & \frac{\partial u_r}{\partial v_{s_1}} & \cdots & \frac{\partial u_r}{\partial v_{s_m}} & \frac{\partial u_r}{\partial \rho_1} & \cdots & \frac{\partial u_r}{\partial \rho_m} \end{bmatrix} * \begin{bmatrix} \Delta v_{p_1} \\ \vdots \\ \Delta v_{p_m} \\ \Delta v_{s_1} \\ \vdots \\ \Delta v_{s_m} \\ \Delta \rho_1 \\ \vdots \\ \Delta \rho_m \end{bmatrix}$$

$$= \begin{bmatrix} \frac{\partial u_1}{\partial v_{p_1}} & \cdots & \frac{\partial u_1}{\partial v_{p_m}} & \frac{\partial u_1}{\partial v_{s_1}} & \cdots & \frac{\partial u_1}{\partial v_{s_m}} & \frac{\partial u_1}{\partial \rho_1} & \cdots & \frac{\partial u_1}{\partial \rho_m} \\ \frac{\partial u_2}{\partial v_{p_1}} & \cdots & \frac{\partial u_2}{\partial v_{p_m}} & \frac{\partial u_2}{\partial v_{s_1}} & \cdots & \frac{\partial u_2}{\partial v_{s_m}} & \frac{\partial u_2}{\partial \rho_1} & \cdots & \frac{\partial u_2}{\partial \rho_m} \\ \vdots & \ddots & \vdots & \vdots & \ddots & \vdots & \vdots & \ddots & \vdots \\ \frac{\partial u_r}{\partial v_{p_1}} & \cdots & \frac{\partial u_r}{\partial v_{p_m}} & \frac{\partial u_r}{\partial v_{s_1}} & \cdots & \frac{\partial u_r}{\partial v_{s_m}} & \frac{\partial u_r}{\partial \rho_1} & \cdots & \frac{\partial u_r}{\partial \rho_m} \end{bmatrix}^T \begin{bmatrix} d_1 - u_1 \\ d_2 - u_2 \\ \vdots \\ d_r - u_r \end{bmatrix} , \quad (4)$$

where m, r, v_P, v_S, and ρ are the total number of elements, the total number of receivers, the P-wave velocity, the S-wave velocity, and the density, respectively.

The frequency domain wave equation in elastic media can be expressed as the linear equation (Marfurt, 1984):

$$\begin{bmatrix} & \mathbf{S}_0 & \end{bmatrix} \begin{bmatrix} u_1 \\ u_2 \\ \vdots \\ u_n \end{bmatrix} = \begin{bmatrix} \mathbf{f} \end{bmatrix} . \quad (5)$$

In eq. (5), $\mathbf{S}_0$ is the complex impedance matrix consisting of the mass matrix and the stiffness matrix, which are constructed from the initial velocity model in the frequency domain. We differentiate eq. (5) with respect to a certain wavefield parameter at an arbitrary point to arrive at

$$\begin{bmatrix} & \mathbf{S}_0 & \end{bmatrix} \begin{bmatrix} \dfrac{\partial u_1}{\partial p_1} \\ \dfrac{\partial u_2}{\partial p_1} \\ \vdots \\ \dfrac{\partial u_n}{\partial p_1} \end{bmatrix} = -\frac{\partial}{\partial p_1} \begin{bmatrix} & \mathbf{S}_0 & \end{bmatrix} \begin{bmatrix} u_1 \\ u_2 \\ \vdots \\ u_n \end{bmatrix} \quad . \tag{6}$$

The right hand side of eq. (6) is assumed to be a virtual-source vector. Furthermore, we can calculate the virtual-source vector in terms of each point and obtain the Jacobian matrix, which is expressed as

$$\begin{bmatrix} \dfrac{\partial u_1}{\partial v_{p_1}} & \cdots & \dfrac{\partial u_1}{\partial v_{p_m}} & \dfrac{\partial u_1}{\partial v_{s_1}} & \cdots & \dfrac{\partial u_1}{\partial v_{s_m}} & \dfrac{\partial u_1}{\partial \rho_1} & \cdots & \dfrac{\partial u_1}{\partial \rho_m} \\ \dfrac{\partial u_2}{\partial v_{p_1}} & \cdots & \dfrac{\partial u_2}{\partial v_{p_m}} & \dfrac{\partial u_2}{\partial v_{s_1}} & \cdots & \dfrac{\partial u_2}{\partial v_{s_m}} & \dfrac{\partial u_2}{\partial \rho_1} & \cdots & \dfrac{\partial u_2}{\partial \rho_m} \\ \vdots & \ddots & \vdots & \vdots & \ddots & \vdots & \vdots & \ddots & \vdots \\ \dfrac{\partial u_r}{\partial v_{p_1}} & \cdots & \dfrac{\partial u_r}{\partial v_{p_m}} & \dfrac{\partial u_r}{\partial v_{s_1}} & \cdots & \dfrac{\partial u_r}{\partial v_{s_m}} & \dfrac{\partial u_r}{\partial \rho_1} & \cdots & \dfrac{\partial u_r}{\partial \rho_m} \end{bmatrix}$$

$$= \begin{bmatrix} & \mathbf{S}_0 & \end{bmatrix}^{-1} \begin{bmatrix} \mathbf{v}(v_{p_1}) & \cdots & \mathbf{v}(v_{p_m}) & \mathbf{v}(v_{s_1}) & \cdots & \mathbf{v}(v_{s_m}) & \mathbf{v}(\rho_1) & \cdots & \mathbf{v}(\rho_m) \end{bmatrix} \quad . \tag{7}$$

Because only surface nodes are needed for the waveform inversion, eq. (7) can be expressed again with the matrix as follows:

$$\mathbf{J} = \mathbf{A}\mathbf{S}_0^{-1}\mathbf{V} \quad , \tag{8}$$

where $\mathbf{A}$ is an r×n matrix:

$$\mathbf{A} = \begin{bmatrix} 1 & 0 & \cdots & 0 & 0 & \cdots & 0 \\ 0 & 1 & \cdots & 0 & 0 & \cdots & 0 \\ \vdots & \vdots & \ddots & \vdots & \vdots & \ddots & \vdots \\ 0 & 0 & \cdots & 1 & 0 & \cdots & 0 \end{bmatrix} \quad , \tag{9}$$

and $\mathbf{V}$ is a matrix comprised of virtual-source vectors:

$$\mathbf{V} = \left[\mathbf{v}(v_{p_1}) \quad \cdots \quad \mathbf{v}(v_{p_m}) \quad \mathbf{v}(v_{s_1}) \quad \cdots \quad \mathbf{v}(v_{s_m}) \quad \mathbf{v}(\rho_1) \quad \cdots \quad \mathbf{v}(\rho_m) \right]. \tag{10}$$

Substituting eq. (8) into eq. (3) gives us the following equation:

$$(\mathbf{A}\mathbf{S}_0^{-1}\mathbf{V})^{\mathrm{T}}(\mathbf{A}\mathbf{S}_0^{-1}\mathbf{V})^{*}\Delta\mathbf{p} = (\mathbf{A}\mathbf{S}_0^{-1}\mathbf{V})^{\mathrm{T}}\mathbf{e}^{*} \ . \tag{11}$$

Because $\mathbf{S}_0$ is a symmetric matrix for elastic media, we can use the property of $(\mathbf{S}_0^{-1})^{\mathrm{T}} = \mathbf{S}_0^{-1}$, and eq. (11) is rewritten as follow:

$$\mathbf{V}^{\mathrm{T}}\mathbf{S}_0^{-1}\mathbf{A}^{\mathrm{T}}\mathbf{A}(\mathbf{S}_0^{-1}\mathbf{V})^{*}\Delta\mathbf{p} = \mathbf{V}^{\mathrm{T}}\mathbf{S}_0^{-1}\mathbf{A}^{\mathrm{T}}\mathbf{e}^{*} \ , \tag{12}$$

which can be more simply expressed as

$$\mathbf{H}\Delta\mathbf{p} = \mathbf{g} \ , \tag{13}$$

when $\mathbf{H} = \mathbf{V}^{\mathrm{T}}\mathbf{S}_0^{-1}\mathbf{A}^{\mathrm{T}}\mathbf{A}(\mathbf{S}_0^{-1}\mathbf{V})^{*}$ and $\mathbf{g} = \mathbf{V}^{\mathrm{T}}\mathbf{S}_0^{-1}\mathbf{A}^{\mathrm{T}}\mathbf{e}^{*}$.

The linear matrix eq. (13) minimizes the objective function using the Gauss-Newton method, and we can solve for from the linear matrix equation by adopting the CGLS method (Golub and Loan, 1996).

Determination of the damping factor

Because the Hessian matrix can be ill-posed, a damping factor should be added to the diagonal elements of the Hessian matrix. To find the proper damping factor, we should know the diagonal elements even though we do not compose the Hessian matrix directly. Therefore, we calculate the damping factor with the following method.

The Hessian value at a particular point can be expressed as

$$\mathrm{H}_{\mathrm{g}} = \mathbf{b}_{\mathrm{i}}^{\mathrm{T}}\mathbf{H}\mathbf{b}_{\mathrm{j}} \ , \tag{14}$$

when $\mathbf{b}_{\mathrm{j}}$ is a unit vector with only a unitary i-th element.

Diagonal elements of the Hessian matrix can be calculated by eq. (14), and the magnitude of the damping factor, λ, can be determined. Then, the damping factor λ is added to each diagonal element of the Hessian matrix.

$$(\mathbf{H} + \lambda\mathbf{I})\Delta\mathbf{p} = \mathbf{H}\Delta\mathbf{p} + \lambda\Delta\mathbf{p} \ . \tag{15}$$

The Hessian matrix can now be calculated stably.

NUMERICAL EXAMPLES

Marmousi-2 velocity model

We performed waveform inversions using the Marmousi-2 model (Martin et al., 2006) to verify our inversion algorithm. The range of the Marmousi-2 model is extended to 17 km from the 9.2 km range of the previous Marmousi model (Versteeg, 1994). The Marmousi-2 reflects more complicated subsurface structures than the Marmousi model, and a 500 m deep layer of water has been added.

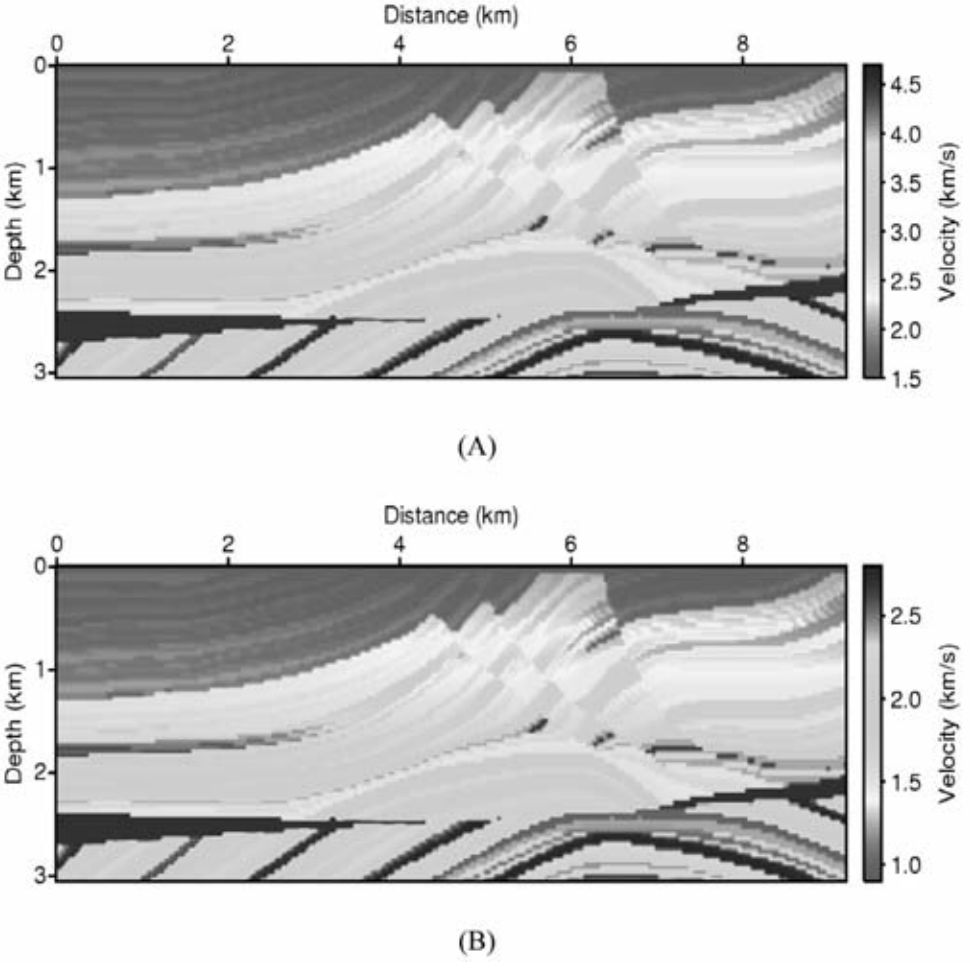

Fig. 1. A velocity model for the modified Marmousi-2 model. (A) is a P-wave velocity model and (B) is a S-wave velocity model.

We designed the P-wave velocity model (Fig. 1a) by reducing the Marmousi-2 model to a 9.2 × 3.04 km model and removing the water layer to speed up the calculation for correctly simulated land conditions. Additionally, we designed a S-wave velocity model (Fig. 1b) for conditions when the Poison ratio is 0.22 because the original S-wave velocity is low enough to cause numerical dispersion unless the grid size is extremely small during high frequency modeling.

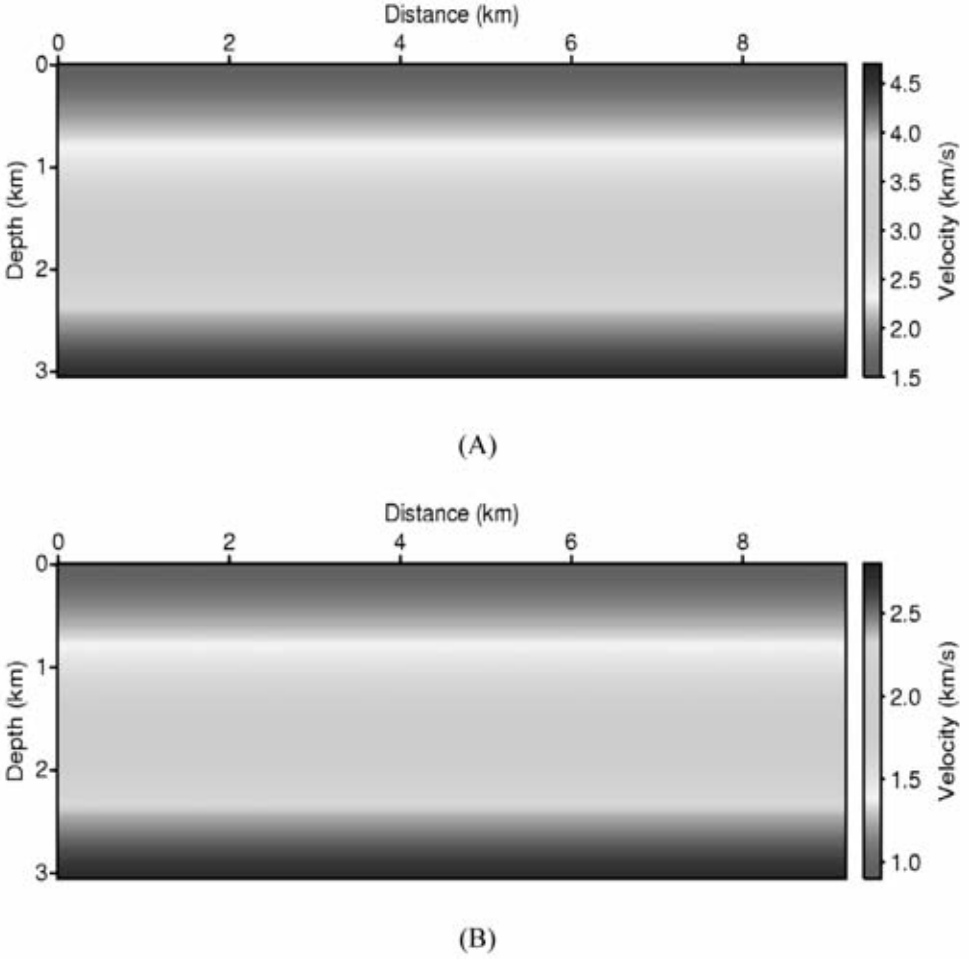

Fig. 2. A linearly increasing initial velocity model. (A) is an initial P-wave velocity model and (B) is an initial S-wave velocity model.

With the modified 40 m interval Marmousi-2 model (Fig. 1), we generated synthetic data from the finite elements method modeling technique and applied the perfectly matched layer (PML) boundary condition in the frequency domain. The source wavelet is the first order differential of the Gaussian function having a maximum frequency of 10 Hz. Receivers were deployed at a 40 m interval over the entire surface, and horizontal and vertical displacements caused by 220 vertical sources were estimated. The total recording time was 6 seconds, and the lowest frequency and the length of the frequency intervals were both 0.1666 Hz.

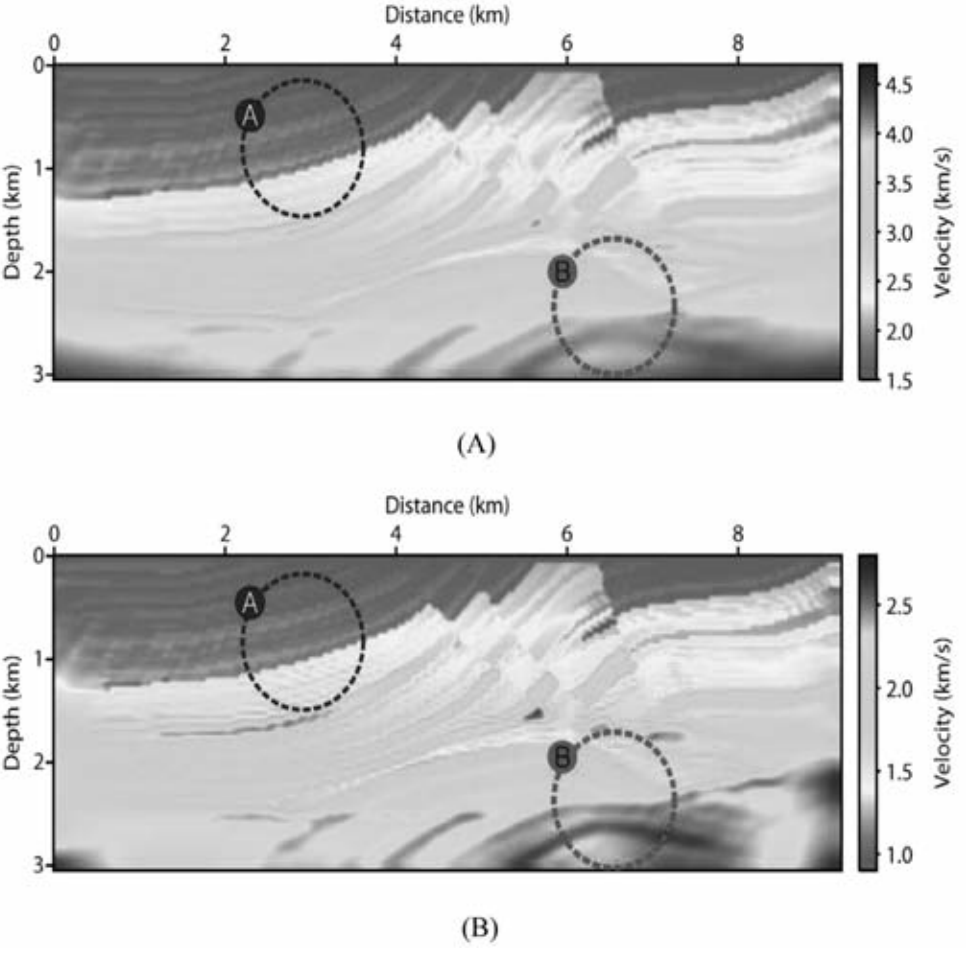

Fig. 3. An inverted velocity model of the Marmousi-2 model using a linearly increasing initial velocity model. (A) is an inverted P-wave velocity model and (B) is an inverted S-wave velocity model.

An inversion method using all the frequency bands at once was applied with a linearly increasing initial velocity model (Fig. 2). Sixty frequencies were used from 0.1666 to 10 Hz at equally spaced interval lengths of 0.1666 Hz. In this setting, P-wave and S-wave velocity models were used as model parameters, and we fixed the density model without updating.

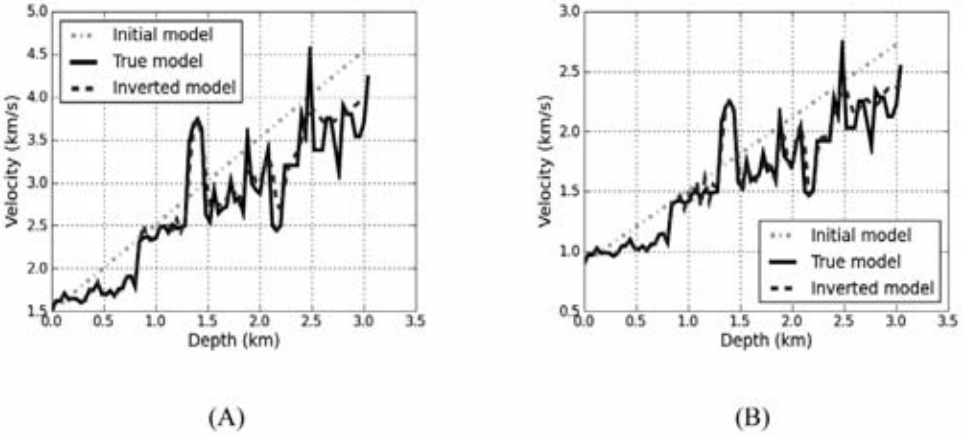

Fig. 4. Velocity profiles of the true model and the inverted model at 3.6 km. They changes with increasing depth. (A) is a P-wave velocity profile and (B) is a S-wave velocity profile.

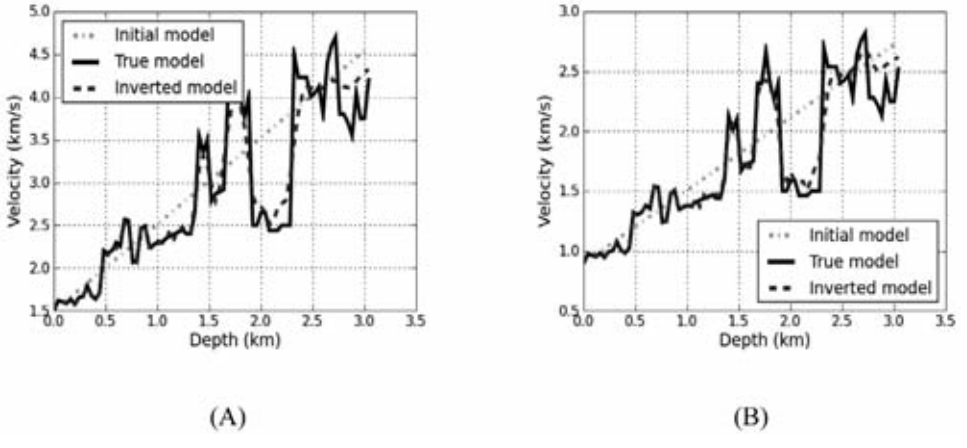

Fig. 5. Velocity profiles of the true model and the inverted model at 7.2 km. They changes with increasing depth. (A) is a P-wave velocity profile and (B) is a S-wave velocity profile.

Despite the fact that linearly increasing velocity models were used as initial models, the inverted velocity models (Fig. 3) successfully identified the complicated shallow structure (location A), and the continuity of the layer is excellent. Furthermore, oil and gas sand cap structure (location B) is obtained, which is a significant result for oil exploration applications.

Velocity profiles of P-wave and S-wave were used for a more accurate analysis, and Figs. 4 and 5 show velocity profiles at 3.6 km and 7.2 km, respectively. All the results indicated the correct inversion from the surface to 2 km, especially the boundary in the high velocity layer at the depth of 1.3 km. At depths deeper than 2.5 km, however, although the inverted model has a similar tendency to the true velocity model, it cannot approximate the true velocity precisely.

SEG/EAGE AA′-line salt model

The SEG/EAGE 3D salt model (Aminzadeh et al., 1997) represents structures containing high velocity salt structure. The presence of a high velocity salt creates serious obstacles in waveform inversion because strong reflections of the elastic wave make it difficult to calculate sub-salt information. We chose the AA′ cross section in the 3D SEG/EAGE velocity model and used it as a P-wave velocity model (Fig. 6a). Additionally, we designed a S-wave velocity model (Fig. 6b) for conditions when the Poison ratio is 0.22 because a true S-wave velocity does not originally exist in this model.

With the modified 40 m interval SEG/EAGE AA′-line model, we generated synthetic data from the finite elements method modeling technique and applied the PML boundary condition in the frequency domain. The source wavelet is the first order differential of the Gaussian function with a maximum frequency of 10 Hz. Receivers were deployed at a 40 m interval across the entire surface, and horizontal and vertical displacements caused by 220 vertical sources were estimated. The total recording time was 6 seconds, and the lowest frequency and the length of the frequency intervals were both 0.1666Hz.

Identical to the previous test for Marmousi-2 velocity model, an inversion method using all the frequency bands at once was applied with a linearly increasing initial velocity model (Fig. 7). Sixty frequencies were used from 0.1666 Hz to 10 Hz at equally spaced interval lengths of 0.1666 Hz. In this setting, P-wave and S-wave velocity models were used as model parameters, and we fixed the density model without updating.

The inverted P-wave (Fig. 8a) and S-wave (Fig. 8b) velocity models clearly identified the shallow layer and the upper part of the salt layer (location A). Furthermore, the thickness of the salt and velocity inside the salt are

calculated accurately, which have been considered a significant problem for waveform inversion in the frequency domain. However, the velocity of the lower part of salt layer converges into excessively low velocity, and it is highly distorted (location B). This problem seems more serious in the inverted S-wave velocity model.

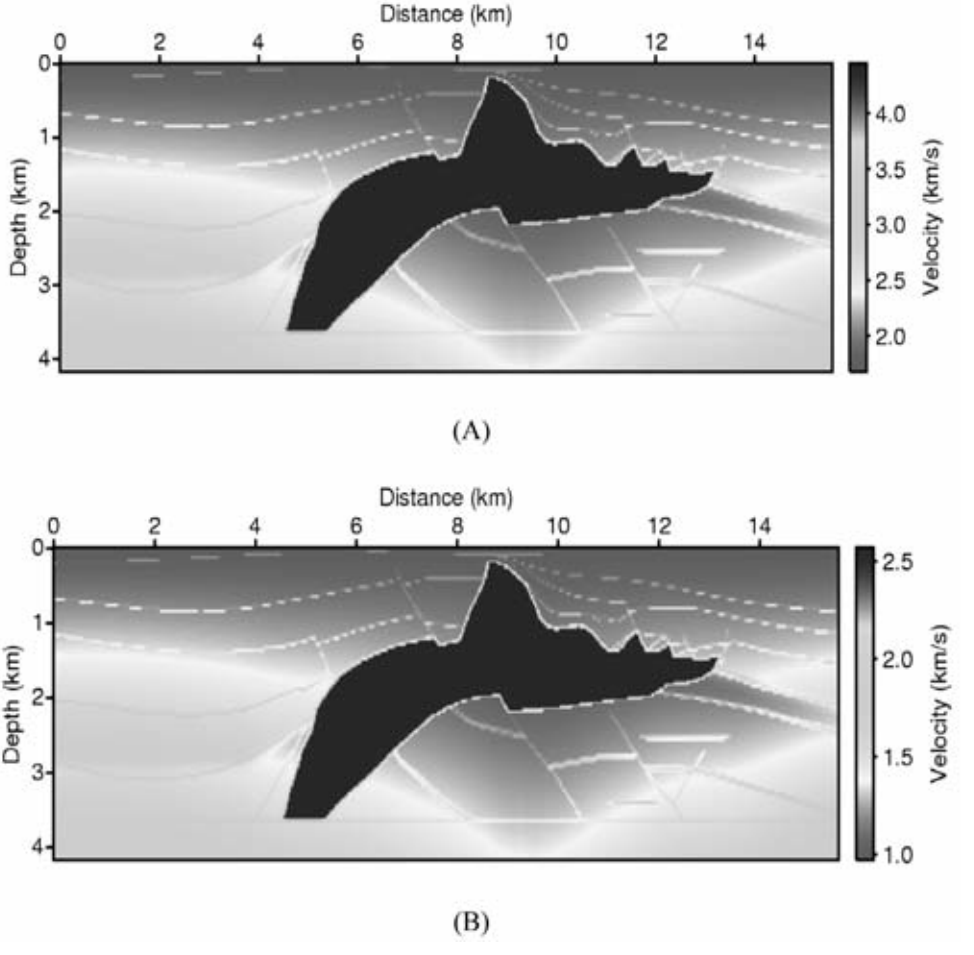

Fig. 6. A velocity model for the SEG/EAGE 3D salt AA′-line. (A) is a P-wave velocity model and (B) is a S-wave velocity model.

Velocity profiles of P-wave and S-wave velocities are used for more accurate analysis. Figs. 9 and 10 show velocity profiles at 8 km and at 12 km, respectively. All the results show the correct high velocity layer where the salt is located, and the tendency of sub-salt velocity is accurately indicated. However, the low velocity layer below the high velocity layer cannot be approximated exactly.

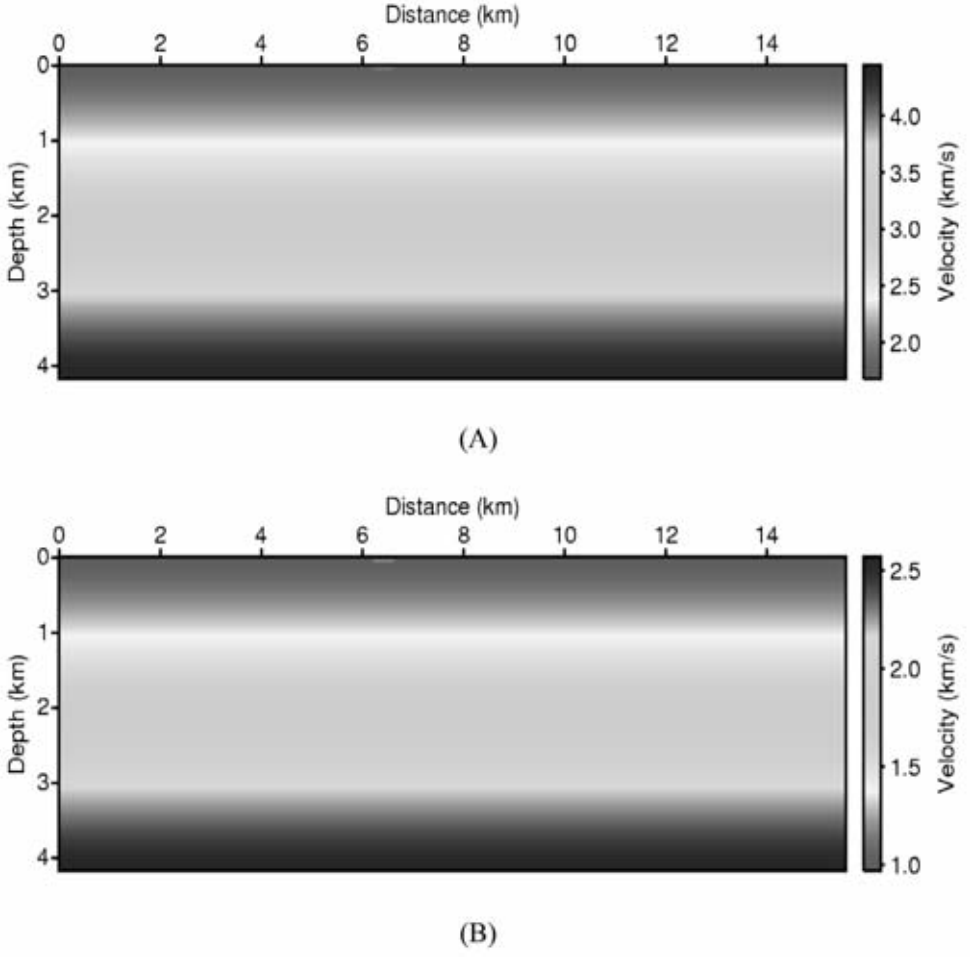

Fig. 7. A linearly increasing initial velocity model. (A) is an initial P-wave velocity model and (B) is an initial S-wave velocity model.

We failed to identify the velocity of the deeper layer correctly with linearly increasing initial velocity models that were used successfully in the Marmousi-2 velocity model inversion. Thus, smoothed true models (Fig. 11) representing the long wavelength characteristic of true models were used as alternative initial models. These initial models were produced using the Seismic Unix utility smooth2 (www.cwp.mines.edu/cwpcodes/). Under the same frequency and parameter settings, waveform inversion was carried out using all the frequency bands at once.

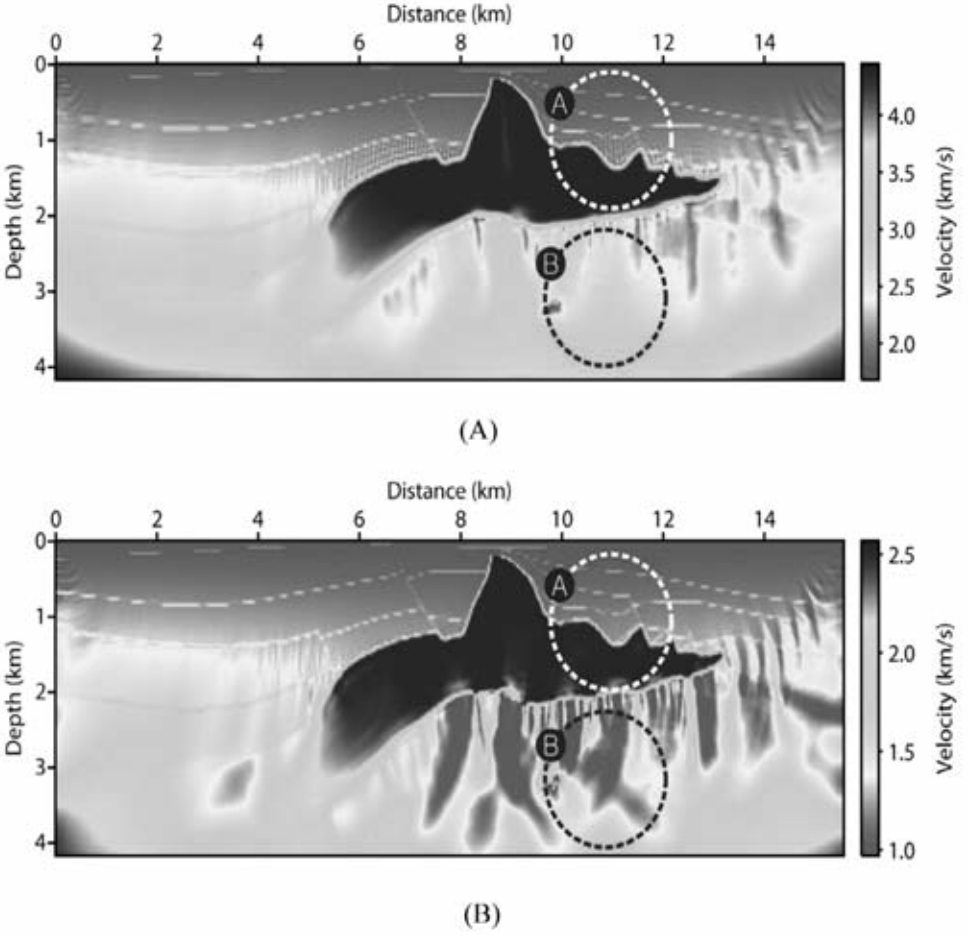

Fig. 8. An inverted velocity model of the SEG/EAGE 3D salt model using a linearly increasing initial velocity model. (A) is an inverted P-wave velocity model and (B) is an inverted S-wave velocity model.

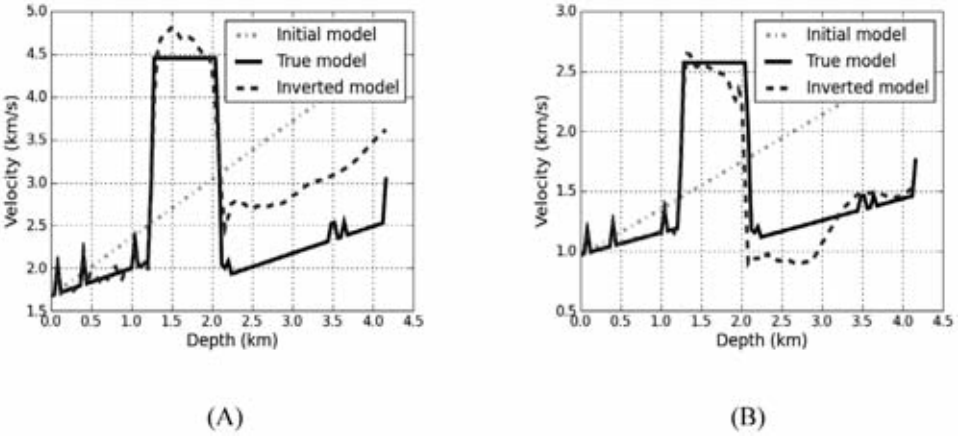

Fig. 9. Velocity profiles of the true model and the inverted model at 8 km. They changes with increasing depth. (A) is a P-wave velocity profile and (B) is a S-wave velocity profile.

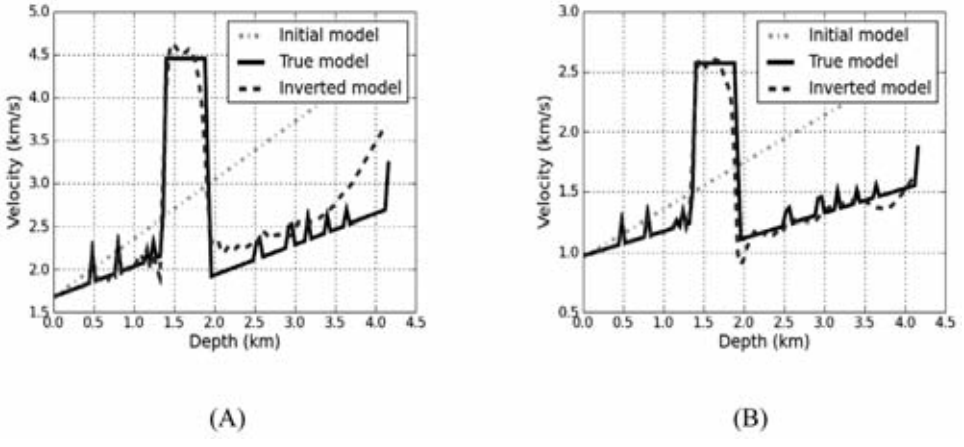

Fig. 10. Velocity profiles of the true model and the inverted model at 12 km. They change with increasing depth. (A) is a P-wave velocity profile and (B) is a S-wave velocity profile.

Unlike the inversion results achieved from using a linearly increasing velocity model as an initial model, the inverted velocity model (Fig. 12) correctly identified deep as well as shallow velocities. The sub-salt lens structure (location A), which is the most useful information in oil exploration, is confirmed exactly.

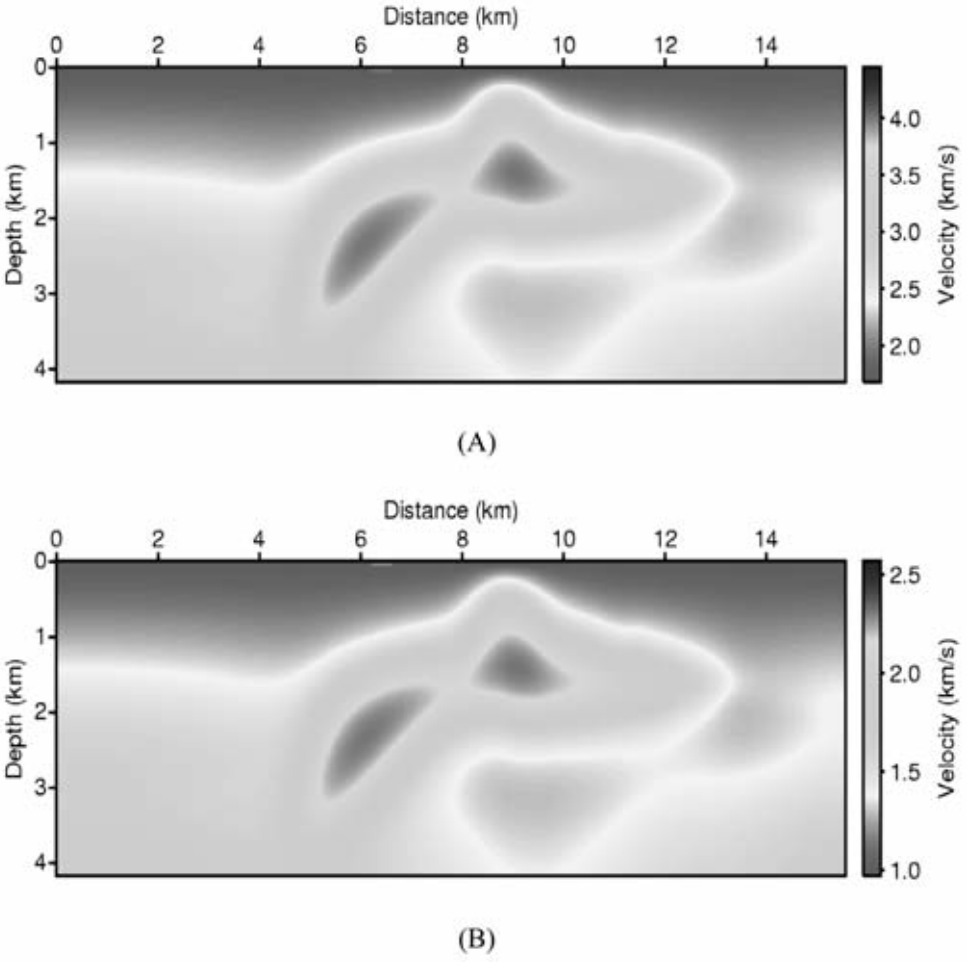

Fig. 11. A smoothed initial velocity model assuming the long wavelength velocity model. (A) is a P-wave velocity model and (B) is a S-wave velocity model.

For a more accurate analysis, velocity profiles are utilized as at an initial stage. Figs. 13 and 14 are velocity profiles at 8 km and at 12 km, respectively. Inversion results inside the salt and below the salt are approximated close to the true velocity models.

In order to demonstrate the superiority of the newly developed Gauss-Newton method of adopting the CGLS algorithm in the SEG/EAGE 3D salt model inversion, we compare the inversion results with those of the conventional Gradient method. The Gradient method, which uses a pseudo-

Hessian without calculating the approximate-Hessian explicitly, has been well studied because of its efficiency. Fig. 15 shows inverted velocity models obtained by the conventional Gradient method. Estimates of the upper layer structure and of structure over the salt area are successful. However, unlike the Gauss-Newton method, the conventional Gradient method failed to identify the velocity model inside the salt correctly. Additionally, the layer below the salt (location A) and the lens structure (location B) were not found by the Gradient method inversion.

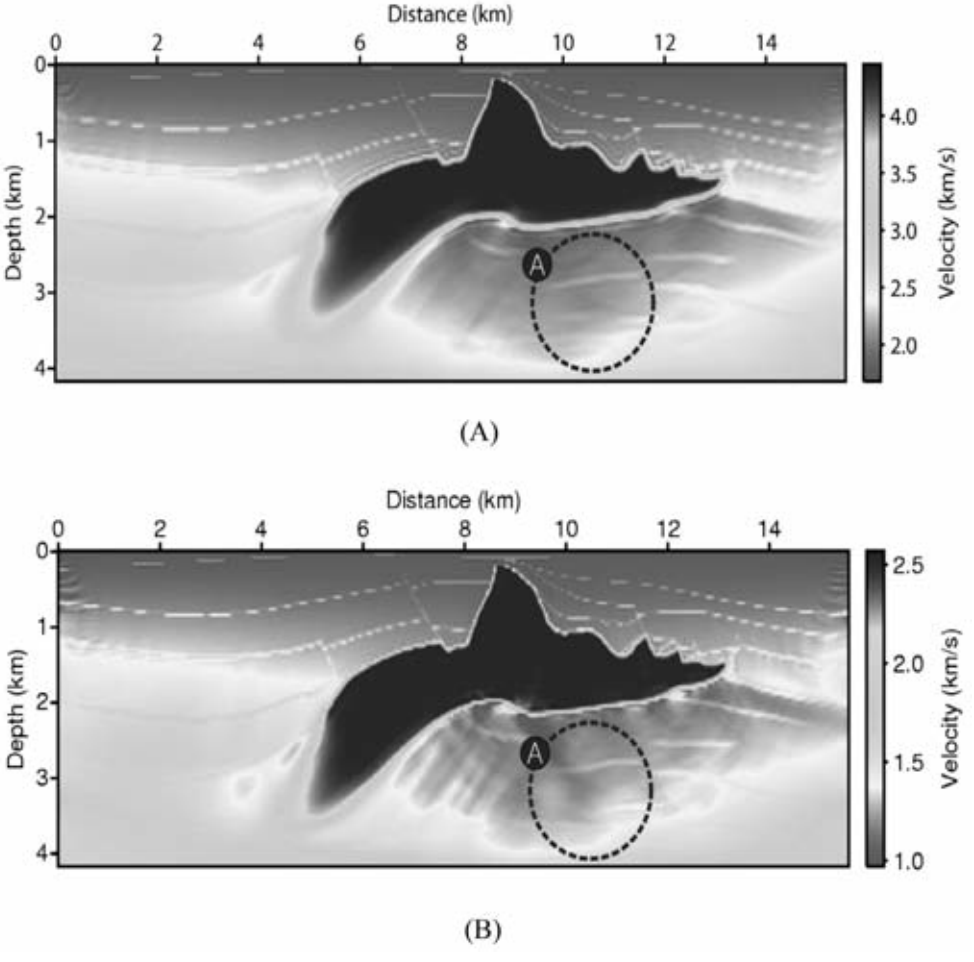

Fig. 12. An inverted velocity model of the SEG/EAGE 3D salt model using a smoothed initial velocity model. (A) is an inverted P-wave velocity model and (B) is an inverted S-wave velocity model.

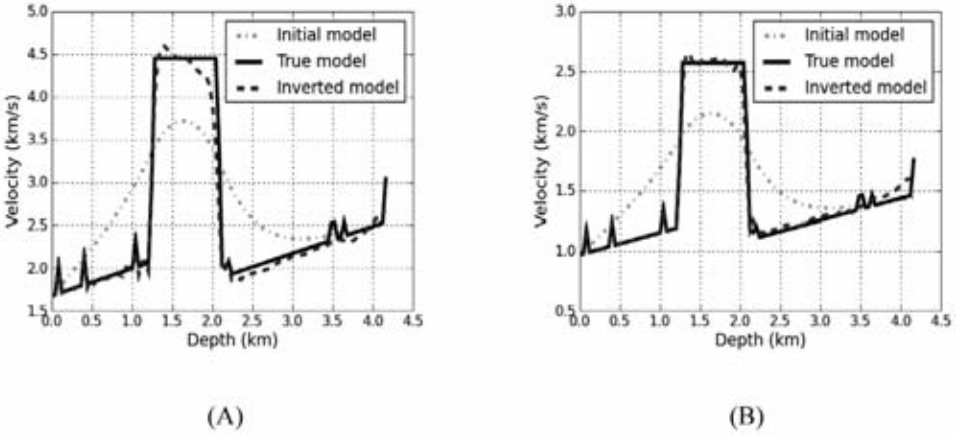

Fig. 13. Velocity profiles of the true model and the inverted model at 8 km. They changes with increasing depth. (A) is a P-wave velocity profile and (B) is a S-wave velocity profile.

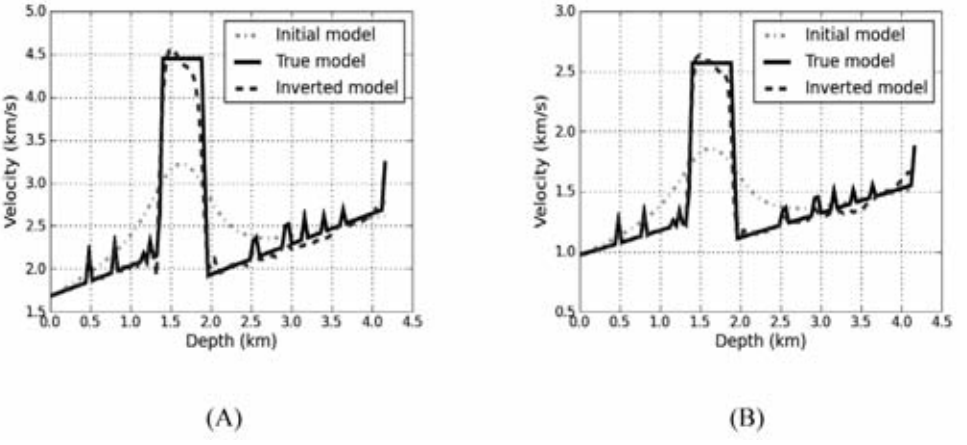

Fig. 14. Velocity profiles of the true model and the inverted model at 12 km. They changes with increasing depth. (A) is a P-wave velocity profile and (B) is a S-wave velocity profile.

CONCLUSION

Although we find an enhanced high-resolution velocity model using the Gauss-Newton method with less iteration, the technique has not been well studied because of the limitations of the current computing environment for calculating Hessian-matrices. Thus, in this study, we adopt the CGLS algorithm to solve the problem of the Hessian-matrix indirectly and develop a frequency domain elastic waveform inversion using the Gauss-Newton method.

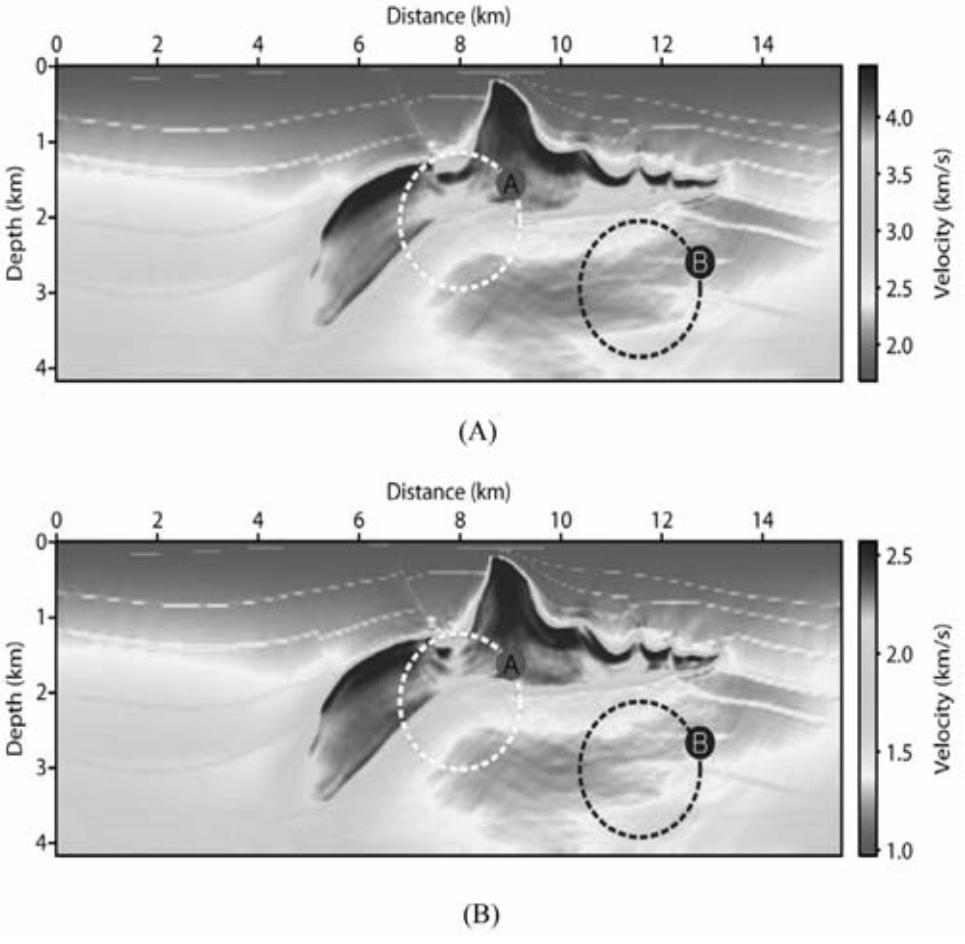

Fig. 15. An inverted velocity model of the SEG/EAGE 3D salt model using the Gradient method. (A) is an inverted P-wave velocity model and (B) is an inverted S-wave velocity model.

We performed numerical experiments with the Marmousi-2 model and SEG/EAGE salt models that are most frequently used for oil exploration. With the Marmousi-2 model, we verified that an inversion of a complicated layer structure can be performed, and with the SEG/EAGE salt model, we confirmed the location and shape of a high velocity salt as well as the P-wave and the S-wave velocity below the salt.

Through numerical experiments with the SEG/EAGE salt model using a linearly increasing velocity model as an initial velocity model, we confirmed that the shallow layer and the thickness of the salt layer could be reproduced perfectly. However, we also detected the distortion of the velocity layer in the

deeper part of the velocity model. Fortunately, this problem is overcome with a different initial velocity model that contains the long wavelength characteristics of the true velocity model. When we perform waveform inversion adopting the CGLS method, we identify underground conditions exactly with the long wavelength velocity model. Therefore, further research is needed to find methods to obtain the long wavelength velocity model.

ACKNOWLEDGEMENTS

This work was supported by the Energy Efficiency & Resources of the Korea Institute of Energy Technology Evaluation and Planning (KETEP) grant funded by the Korea government Ministry of Knowledge Economy (No. 2010T100200376)

REFERENCES

Aminzadeh, F., Brac, J. and Kunz, T., 1997. 3-D Modeling Series No.1: 3-D Salt and Overthrust Models. SEG, Tulsa, OK and EAGE, Houten.

Chen, P., Jordan, T.H. and Zhao, L., 2007. Full three-dimensional tomography: a comparison between the scattering-integral and adjoint-wavefield methods. Geophys. J. Internat., 170: 175-181.

Epanomeritakis, I., Akcelik, V., Ghattas, O. and Bielak, J., 2008. A Newton-CG method for large-scale three dimensional elastic full-waveform seismic inversion. Inverse Probl., 24: 034015.

Golub, G.H. and Van Loan, C.F., 1996. Matrix Computation, 3rd Ed. The Johns Hopkins University Press, Baltimore.

Hu, W., Abubakar, A. and Habashy, T.M., 2009. Simultaneous multifrequency inversion of full-waveform seismic data. Geophysics, 74: R1-R14.

Kolb, P., Collino, F. and Lailly, P., 1986. Pre-stack inversion of a 1-D medium. Proc. IEEE, 74: 498-508.

Lailly, P., 1983. The seismic inverse problem as a sequence of before stack migrations. In: Bednar, J.B. (Ed.), Conference on Inverse Scattering: Theory and Application. University of Tulsa, OK: 206-220.

Marfurt, K.J., 1984. Accuracy of finite-difference and finite-element modeling of the scalar and elastic wave equations. Geophysics, 49: 533-549.

Martin, G.S., Wiley, R. and Marfurt, K.J., 2006. Marmousi-2: An elastic upgrade for Marmousi. The Leading Edge, 25: 156-166.

Mora. P., 1987. Nonlinear two-dimensional elastic inversion of multioffset seismic data. Geophysics, 52: 1211-1228.

Pratt, R.G., Shin, C.S. and Hicks, G.J., 1998. Gauss-Newton and full Newton methods in frequency-space seismic waveform inversion. Geophys. J. Internat., 133: 341-362.

Shin, C.S., Pyun, S. and Bednar, J.B., 2007. Comparison of waveform inversion, Part 1: Conventional wavefield vs. logarithmic wavefield. Geophys. Prosp., 55: 449-464.

Shin, C.S. and Min, D.J., 2006. Waveform inversion using a logarithmic wavefield. Geophysics, 71: R31-R42.

Tarantola, A., 1984. Inversion of seismic reflection data in the acoustic approximation. Geophysics, 49: 1259-1266.

Versteeg, R., 1994. The Marmousi experience: Velocity model determination on a synthetic complex data set. The Leading Edge, 13: 927-936.